

1 **Tropopause Evolution in a Rapidly Intensifying Tropical Cyclone: A Static**
2 **Stability Budget Analysis in an Idealized, Axisymmetric Framework**

3 Patrick Duran* and John Molinari

4 *University at Albany, State University of New York, Albany, NY*

5 **Corresponding author address:* Department of Atmospheric and Environmental Sciences, Univer-
6 sity at Albany, State University of New York, 1400 Washington Avenue, Albany, NY.

7 E-mail: pduran2008@gmail.com

ABSTRACT

8 Large changes in tropopause-layer static stability are observed during the
9 rapid intensification (RI) of an idealized, axisymmetric tropical cyclone (TC).
10 Over the eye, static stability near the tropopause decreases and the cold-point
11 tropopause height rises by up to 4 km at the storm center. Outside of the eye,
12 static stability increases considerably just above the cold-point tropopause,
13 and the tropopause remains near its initial level.

14 A budget analysis reveals that advection contributes to the static stability
15 tendencies at all times throughout the upper troposphere and lower strato-
16 sphere. Differential advection is particularly important within the eye, where
17 it acts to destabilize the layer near and above the cold-point tropopause.
18 Outside of the eye, a radial-vertical circulation develops during RI, with
19 strong outflow below the tropopause and weak inflow above. Vertical wind
20 shear above and below the upper-tropospheric outflow maximum induces tur-
21 bulence, which provides forcing for both destabilization and stabilization
22 in the tropopause layer. Meanwhile, as organized convection reaches the
23 tropopause, radiative heating tendencies at the top of the cirrus canopy gen-
24 erally act to destabilize the upper troposphere and stabilize the lower strato-
25 sphere. Turbulent mixing and radiative heating combine to play an important
26 role in the development of the strong stable layer immediately above the cold-
27 point tropopause during RI. The results suggest that turbulence and radiation,
28 alongside advection, play fundamental roles in the upper-level static stability
29 evolution of TCs.

30 **1. Introduction**

31 After undergoing a remarkably rapid intensification (RI), Hurricane Patricia (2015) set a new
32 record as the strongest tropical cyclone (TC) ever observed in the Western Hemisphere (Kim-
33 berlain et al. 2016; Rogers et al. 2017). High-altitude dropsonde observations taken during the
34 Tropical Cyclone Intensity (TCI) experiment captured this RI in unprecedented detail (Doyle et al.
35 2017). These observations revealed dramatic changes in the structure of the cold-point tropopause
36 and upper-level static stability as the storm intensified (Duran and Molinari 2018).

37 At tropical storm intensity, shortly before RI commenced, a strong inversion layer existed just
38 above the cold-point tropopause. During the first half of the RI period, this inversion layer weak-
39 ened throughout Patricia’s inner core, with the weakening most pronounced over the developing
40 eye. By the time the storm reached its maximum intensity of 95 m s^{-1} , the inversion layer over
41 the eye had disappeared almost completely, which was accompanied by a greater than 1-km in-
42 crease in the tropopause height. Meanwhile over the eyewall region, the static stability increased
43 and the tropopause remained near its initial level. The mechanisms that might have led to this
44 tropopause-layer variability will be investigated in the current paper using idealized simulations.

45 Despite the importance of tropopause-layer thermodynamics in theoretical models of hurri-
46 canes (Emanuel and Rotunno 2011; Emanuel 2012), most observational studies of the upper-
47 tropospheric structure of TCs are decades old. Recently, however, Komaromi and Doyle (2017)
48 found that stronger TCs tended to have a higher and warmer tropopause over their inner core than
49 weaker TCs. Their results are consistent with the evolution observed over the inner core of Hur-
50 ricane Patricia, in which the tropopause height increased and the tropopause temperature warmed
51 throughout RI (Duran and Molinari 2018).

52 Idealized simulations of a TC analyzed by Ohno and Satoh (2015) suggested that the develop-
53 ment of an upper-level warm core near the 13-km level acted to decrease the static stability near the
54 tropopause within the eye (compare their Figs. 9,10). Although the mechanisms that might drive
55 this static stability evolution have not been examined explicitly, Stern and Zhang (2013) described
56 the development of the TC warm core using a potential temperature (θ) budget analysis. They
57 found that radial and vertical advection both played important roles in warm core development
58 throughout RI, and subgrid-scale diffusion became particularly important during the later stage of
59 RI. To our knowledge, the only paper that has examined explicitly the static stability evolution in
60 a modeled TC is Kepert et al. (2016), but their analysis was limited to the boundary layer. The
61 analysis herein is based upon that of Stern and Zhang (2013), except using a static stability budget
62 similar to that of Kepert et al. (2016), with a focus on the upper troposphere and lower stratosphere.

63 **2. Model Setup**

64 The numerical simulations were performed using version 19.4 of Cloud Model 1 (CM1) de-
65 scribed in Bryan and Rotunno (2009). The equations of motion were integrated on a 3000-km-
66 wide, 30-km-deep axisymmetric grid with 1-km horizontal and 250-m vertical grid spacing. The
67 computations were performed on an f -plane at 15°N latitude, over a sea surface with constant
68 temperature of 30.5°C, which matches that observed near Hurricane Patricia (2015; Kimberlain
69 et al. 2016). Horizontal turbulence was parameterized using the Smagorinsky scheme described
70 in Bryan and Rotunno (2009, pg. 1773), with a prescribed mixing length that varied linearly from
71 100 m at a surface pressure of 1015 hPa to 1000 m at a surface pressure of 900 hPa. Vertical
72 turbulence was parameterized using the formulation of Markowski and Bryan (2016, their Eq. 6),
73 using an asymptotic vertical mixing length of 100 m. A Rayleigh damping layer was applied out-
74 side of the 2900-km radius and above the 25-km level to prevent spurious gravity wave reflection

at the model boundaries. Microphysical processes were parameterized using the Thompson et al. (2004) scheme and radiative heating tendencies were computed every two minutes using the Rapid Radiative Transfer Model for GCMs (RRTMG) longwave and shortwave schemes (Iacono et al. 2008). The initial temperature and humidity field was horizontally homogeneous and determined by averaging all Climate Forecast System Reanalysis (CFSR) grid points within 100 km of Patricia's center of circulation at 18 UTC 21 October 2015. The vortex described in Rotunno and Emanuel (1987, their Eq. 37) was used to initialize the wind field, setting all parameters equal to the values used therein.

Although hurricanes simulated in an axisymmetric framework tend to be more intense than those observed in nature, the intensity evolution of this simulation matches reasonably well with that observed in Hurricane Patricia. After an initial spin-up period of about 20 hours, the modeled storm (Fig.1, blue lines) began an RI period that lasted approximately 30 hours. After this RI, the storm continued to intensify more slowly until the maximum 10-m wind speed reached 89 m s^{-1} and the minimum sea-level pressure reached its minimum of 846 mb, 81 hours into the simulation. Hurricane Patricia (red stars) exhibited a similar intensity evolution prior to its landfall, with an RI period leading to a maximum 10-m wind speed of 95 m s^{-1} and a minimum sea-level pressure of 872 hPa.

3. Budget Computation

The static stability can be expressed as the squared Brunt-Väisälä frequency:

$$N_m^2 = \frac{g}{T} \left(\frac{\partial T}{\partial z} + \Gamma_m \right) \left(1 + \frac{T}{R_d/R_v + q_s} \frac{\partial q_s}{\partial T} \right) - \frac{g}{1 + q_t} \frac{\partial q_t}{\partial z}, \quad (1)$$

where g is gravitational acceleration, T is temperature, R_d and R_v are the gas constants of dry air and water vapor, respectively, q_s is the saturation mixing ratio, q_t is the total condensate mixing

ratio, and Γ_m is the moist-adiabatic lapse rate:

$$\Gamma_m = g(1 + q_t) \left(\frac{1 + L_v q_s / R_d T}{c_{pm} + L_v \partial q_s / \partial T} \right), \quad (2)$$

where L_v is the latent heat of vaporization and c_{pm} is the specific heat of moist air at constant pressure. In the tropopause layer, q_s , $\partial q_s / \partial T$, and $\partial q_t / \partial z$ approach zero. In this limiting case, Eq. 1 reduces to:

$$N^2 = \frac{g}{\theta} \frac{\partial \theta}{\partial z}, \quad (3)$$

where θ is the potential temperature.

To compute N^2 , CM1 uses Eq. 1 in saturated environments and Eq. 3 in sub-saturated environments. For simplicity, however, only Eq. 3 will be employed for the budget computations¹.

Taking the time derivative of Eq. 3 yields the static stability tendency:

$$\frac{\partial N^2}{\partial t} = \frac{g}{\theta} \frac{\partial}{\partial z} \frac{\partial \theta}{\partial t} - \frac{g}{\theta^2} \frac{\partial \theta}{\partial z} \frac{\partial \theta}{\partial t}, \quad (4)$$

where the potential temperature tendency, $\partial \theta / \partial t$, can be written, following Bryan (cited 2018):

$$\frac{\partial \theta}{\partial t} = -u \frac{\partial \theta}{\partial r} - w \frac{\partial \theta}{\partial z} + HTURB + VTURB + MP + RAD + DISS \quad (5)$$

Each term on the right-hand side of Eq. 5 represents a θ budget variable, each of which is output directly by the model every minute. Since the first term on the right-hand side of Eq. 4 is larger than the second term throughout most of the tropopause layer (not shown), the contribution of each of the terms in Eq. 5 to the N^2 tendency can be interpreted in light of a vertical gradient of each term.

Taking the vertical gradient of the first two terms on the right-hand side yields the time tendency of the vertical θ gradient due to horizontal and vertical advection²:

¹The validity of this approximation will be substantiated later in this section.

²These terms include the tendencies due to implicit diffusion in the fifth-order finite differencing scheme, which are separated from the advection

terms in the CM1 budget output

$$\left(\frac{\partial}{\partial t} \frac{\partial \theta}{\partial z} \right)_{adv} = -u \frac{\partial}{\partial r} \frac{\partial \theta}{\partial z} - w \frac{\partial}{\partial z} \frac{\partial \theta}{\partial z} - \frac{\partial u}{\partial z} \frac{\partial \theta}{\partial r} - \frac{\partial w}{\partial z} \frac{\partial \theta}{\partial z}. \quad (6)$$

112 The first two terms on the right-hand side of Eq. 6 represent advection of static stability by the
 113 radial and vertical wind, respectively. These terms act to rearrange the static stability field, but
 114 cannot strengthen or weaken static stability maxima or minima. The third and fourth terms on the
 115 right-hand side of Eq. 6 represent, respectively, the tilting of isentropes in the presence of vertical
 116 wind shear and the stretching or squashing of isentropes by vertical gradients of vertical velocity.
 117 Since these terms involve velocity gradients, they can act to strengthen or weaken static stability
 118 maxima or minima through differential advection. For example, since the θ of the air flowing
 119 out of the eyewall into the upper-tropospheric outflow layer increases as the TC intensifies, θ in-
 120 creases locally within the outflow layer. This acts to increase $\partial \theta / \partial z$ below the outflow maximum
 121 and decrease $\partial \theta / \partial z$ above, thereby modifying the static stability field. Similarly, the decay of
 122 updrafts with height at the top of convective towers can act to increase $\partial \theta / \partial z$ through squashing
 123 of isentropes.

124 Returning to Eq. 5, HTURB and VTURB are the tendencies from the horizontal and vertical
 125 turbulence parameterizations, MP is the tendency from the microphysics scheme, RAD is the
 126 tendency from the radiation scheme, and DISS is the tendency due to turbulent dissipation. This
 127 equation neglects Rayleigh damping, since the entire analysis domain is outside of the regions
 128 where damping is applied. Each term in Eq. 5 is substituted for $\partial \theta / \partial t$ in Eq. 4, yielding the
 129 contribution of each budget term to the static stability tendency. These terms are summed, yielding
 130 an instantaneous "budget change" in N^2 every minute. The budget changes are then averaged over
 131 24-hour periods and compared to the total model change in N^2 over that same time period, i.e.:

$$\Delta N_{budget}^2 = \frac{1}{\delta t} \sum_{t=t_0}^{t_0+\delta t} \frac{\partial N^2}{\partial t} \Big|_t \quad (7)$$

$$\Delta N_{model}^2 = N_{t_0+\delta t}^2 - N_{t_0}^2 \quad (8)$$

$$Residual = \Delta N_{model}^2 - \Delta N_{budget}^2 \quad (9)$$

where t_0 is an initial time and δt is 24 hours.

Eqs. 7-9 are plotted for three consecutive 24-hour periods in Fig. 2. For this and all subsequent radial-vertical cross sections, a 1-2-1 smoother is applied once in the radial direction to eliminate $2\Delta r$ noise that appears in some of the raw model output and calculated fields. The left column of Fig. 2 depicts the model changes computed using Eq. 8, along with Eq. 1 in saturated environments and Eq. 3 in subsaturated environments. The center column depicts the budget changes computed using Eq. 7 along with Eq. 3 throughout the domain. Thus, the left column includes the effect of moisture in the N^2 computations, whereas the center column neglects moisture. The right column depicts the residuals, computed using Eq. 9 (i.e. the left column minus the center column.) In every 24-hour period, the budget changes are nearly identical to the model changes, which is reflected in the near-zero residuals in the right column. This indicates that the budget accurately represents the model variability, which implies that the neglect of moisture in the budget computation introduces negligible error within the analysis domain³.

In the tropopause layer, some of the budget terms are small enough to be ignored. To determine which of the budget terms are most important, a time series of the contribution of each of the budget terms in Eq. 5 to the tropopause-layer static stability tendency is plotted in Fig. 3. For this figure, each of the budget terms is computed using the method described in Section 3, except with 1-hour averaging intervals instead of 24-hour intervals. The absolute values of these tendencies are then averaged over the radius-height domain of the plots shown in Fig. 2 and plotted as a time

³This is not the case in the lower- and mid-troposphere, where the residual actually exceeds the budget tendencies in many places, likely due to the neglect of moisture; thus we limit this analysis to the upper troposphere and lower stratosphere.

153 series⁴. Advection (Fig. 3, red line) plays an important role in the mean tropopause-layer static
154 stability tendency at all times, and vertical turbulence (Fig. 3, blue line) and radiation (Fig. 3, dark
155 green line) also contribute significantly. The remaining three processes - horizontal turbulence,
156 microphysics, and dissipative heating - lie atop one another near zero. Although the horizontal
157 turbulence and microphysics terms can be quite large in the eyewall region, they are negligible
158 everywhere outside of the eyewall, and do not play important roles in the mesoscale tropopause
159 variability. Dissipative heating, meanwhile, is relatively small everywhere.

160 The preceding analysis indicates that, at all times, three budget terms dominate the tropopause-
161 layer static stability tendency: advection, vertical turbulence, and radiation. Variations in the
162 magnitude and spatial structure of these terms drive the static stability changes depicted in Fig. 2;
163 subsequent sections will focus on these variations and what causes them.

164 4. Results

165 a. Static stability evolution

166 The average N^2 over the first day of the simulation (Fig. 4a) indicates the presence of a weak N^2
167 maximum just above the cold-point tropopause. Over the subsequent 24 hours, during the RI pe-
168 riod, the N^2 within and above this layer decreased near the storm center (Fig. 4b). This decreasing
169 N^2 corresponded to an increase in the tropopause height within the developing eye, maximized at
170 the storm center. Outside of the eye, meanwhile, the tropopause height decreased over the eyewall
171 region (25-60-km radius) and increased only slightly outside of the 60-km radius. In this outer
172 region, the N^2 maximum just above the tropopause strengthened during RI. These trends contin-

⁴It will be seen in subsequent figures that each of the terms contributes both positively and negatively to the N^2 tendency within the analysis domain. Thus, taking an average over the domain tends to wash out the positive and negative contributions. To circumvent this problem, the absolute value of each of the terms is averaged.

173 ued as the storm's intensity leveled off in the 48-72-hour period (Fig. 4c). The tropopause height
174 increased to nearly 21 km at the storm center and sloped sharply downward to 16.3 km on the
175 inner edge of the eyewall, near the 30 km radius. Static stability outside of the eye, meanwhile,
176 continued to increase just above the cold-point tropopause. This N^2 evolution closely follows that
177 observed in Hurricane Patricia (2015; Duran and Molinari 2018). The mechanisms that led to
178 these N^2 changes will be investigated in the subsequent sections.

179 *b. Static stability budget analysis*

180 *(i) 0-24 hours* The weakening of the lower-stratospheric N^2 maximum during the initial spin-up
181 period is reflected in the total N^2 budget change over this time (Fig. 5a). The layer just above
182 the cold-point tropopause was characterized by decreasing N^2 (purple shading), maximizing at the
183 storm center. At and immediately below the tropopause, meanwhile, saw increasing N^2 during this
184 time period. Although these tendencies extended out to the 200-km radius, they were particularly
185 pronounced at innermost radii. A comparison of the contributions of advection (Fig. 5b), vertical
186 turbulence (Fig. 5c), and radiation (Fig. 5d) reveals that advection was the primary driver of the
187 N^2 tendency during this period, acting to stabilize near and just below the tropopause and destabi-
188 lize above. Although vertical turbulence acted in opposition to advection (i.e. it acted to stabilize
189 regions that advection acted to destabilize), the magnitude of the advective tendencies was larger,
190 particularly at the innermost radii. The sum of advection and vertical turbulence (Fig. 5e) almost
191 exactly replicated the static stability tendencies above the tropopause. Radiative tendencies, mean-
192 while, (Fig. 5d) acted to destabilize the layer below about 16 km and stabilize the layer between
193 16 and 17 km. The sum of advection, vertical turbulence, and radiation (Fig. 5f) reproduces the
194 total change in N^2 almost exactly.

195 (ii) *24-48 hours* During the RI period, N^2 within the eye generally decreased above 16 km and
196 increased below (Fig. 6a), with the destabilization above 16 km maximizing near the level of the
197 mean cold-point tropopause. These tendencies at the innermost radii were driven almost entirely
198 by advection (Fig. 6b); vertical turbulence (Fig. 6c) and radiation (Fig. 6d) contributed negligibly
199 to the static stability tendencies in this region.

200 Outside of the eye, the N^2 evolution exhibited alternating layers of positive and negative tenden-
201 cies. Near and above 18 km existed an upward-sloping region of decreasing N^2 that extended out
202 to the 180-km radius. In this region, neither vertical turbulence nor radiation exhibited negative N^2
203 tendencies; advection was the only forcing for this destabilization. Immediately below this layer,
204 just above the cold-point tropopause, was a region of increasing N^2 that sloped upward from 17 km
205 near the 30-km radius to just below 18 km outside of the 100-km radius. Advection and vertical
206 turbulence both contributed to this positive N^2 tendency, with advection playing an important role
207 below about 17.5 km and and turbulence playing an important role above. The sum of advection
208 and turbulence (Fig. 6e) reveals two discontinuous regions of increasing N^2 in the 17-18-km layer
209 rather than one contiguous region. The addition of radiation to these two terms, however, (Fig. 6f)
210 provides the link between these two regions, indicating that radiation also plays a role in strength-
211 ening the stable layer just above the tropopause. In the 16-17-km layer, just below the cold-point
212 tropopause, a horizontally-extensive layer of destabilization also was forced by a combination of
213 advection, vertical turbulence, and radiation. The sum of advection and vertical turbulence ac-
214 counts for only a portion of the decreasing N^2 in this layer, and actually indicates forcing for
215 stabilization near the 50-km radius and outside of the 130-km radius. Radiative tendencies over-
216 come this forcing for stabilization in both of these regions to produce the radially-extensive region
217 of destabilization observed just below the tropopause.

218 The sum of advection, vertical turbulence, and radiation (Fig. 6f) once again closely follows
219 the observed N^2 variability, except in the eyewall region, where the neglect of latent heating and
220 horizontal turbulence introduces some differences.

221 (iii) 48-72 hours After the storm's maximum wind speed leveled off near 80 m s^{-1} , the magnitude
222 of the static stability tendencies within the eye decreased to near zero (Fig. 7a).

223 Outside of the eye, however, N^2 continued to decrease at and just below the tropopause and
224 increase above it. The sum of advection and vertical turbulence (Fig. 7e) indicates that the increase
225 of N^2 observed in the 17-18-km layer and inside of the 80-km radius cannot be attributed to these
226 processes, since the sum of these two terms provided forcing for destabilization. Instead, radiation
227 (Fig. 7d), provided the forcing for stabilization in this region. Outside of the 80-km radius, both
228 advection (Fig. 7b) and vertical turbulence (Fig. 7c) provided forcing for stabilization near the
229 18-km level. The sum of the two terms (Fig. 7e) indicates increasing N^2 near the 18-km level
230 everywhere outside of the 80-km radius, but this stabilization is slightly weaker in the 90-120-km
231 radial band than the observed value. The addition of radiation (Fig. 7f) provides the extra forcing
232 for stabilization required to account for the observed increase in N^2 . Outside of the 120-km radius,
233 the region of radiative forcing for stabilization slopes downward, and the increase in N^2 observed
234 near 18 km can be explained entirely by a combination of advection and vertical turbulence. The
235 layer of decreasing N^2 observed near the tropopause was forced primarily by vertical turbulence
236 and radiation. Within most of this region, advection provided strong forcing for stabilization, but
237 this forcing was outweighed by the negative N^2 tendencies induced by a combination of vertical
238 turbulence and radiation.

5. Discussion

a. The role of advection

Advection played an important role in the tropopause-layer N^2 evolution at all stages of intensification, but for brevity, this section will focus only on the RI (24-48-hour) period. To investigate the advective processes more closely, the individual contributions of horizontal and vertical advection during the RI period are shown in Fig. 8, along with the corresponding time-mean radial and vertical velocities and θ . The N^2 tendencies due to the two advective components (Fig. 8a,b) exhibit strong cancellation, consistent with flow that is nearly isentropic. There are, however, many regions in which flow crosses θ surfaces; this flow accounts for all non-zero N^2 tendencies due to advection previously seen in Fig. 6b.

During the RI period, strong radial and vertical circulations developed near the tropopause (Fig. 8c,d), which forced high-magnitude N^2 tendencies due to advection (Fig. 8a,b). A layer of strong outflow formed at and below the tropopause during this period, with the outflow maximum (dashed cyan line) curving from the 14-km level at the 50-km radius to just below the 16-km level outside of the 80-km radius (Fig. 8c). Notably, the N^2 tendency due to horizontal advection (Fig. 8a) tended to switch signs at this line, with stabilization below the outflow maximum and destabilization above. Outside of the eye and eyewall, isentropes generally sloped upward with radius. Vertical wind shear acting on these upward-sloping isentropes should act to tilt them into the vertical above the outflow maximum, thereby decreasing $\partial\theta/\partial z$, and tilt them to be more horizontal below the outflow maximum, thereby increasing $\partial\theta/\partial z$. This mechanism is the same as that discussed in Trier and Sharman (2009), and is consistent with the change in sign of the N^2 tendency at the level of maximum outflow.

261 Meanwhile in the lower stratosphere, a thin layer of 2-4 m s⁻¹ inflow developed a few hundred
 262 meters above the tropopause, similar to that which was observed in Hurricane Patricia (2015; Du-
 263 ran and Molinari 2018) and in previous modeling studies (e.g. Ohno and Satoh 2015; ? ?). Since
 264 the isentropes in this layer sloped slightly upward with radius (i.e. $\partial\theta/\partial r < 0$), this inflow acted
 265 to import lower θ air from outer radii to inner radii. Since the negative θ tendencies maximized
 266 at the level of maximum inflow, the layer below the inflow maximum destabilized and the layer
 267 above stabilized (Fig. 8a).

268 Curiously, horizontal advection contributed to the N^2 tendency everywhere within the eye, even
 269 though the mean radial velocity was near zero. Close examination of the model output revealed
 270 that these tendencies were forced by advective processes associated with inward-propagating
 271 waves. Although the radial velocity perturbations induced by these waves averaged out to zero, the
 272 advective tendencies forced by the radial velocity perturbations did not. Additionally, when these
 273 waves reached $r=0$, a dipole of vertical velocity resulted, with ascent above and descent below. For
 274 reasons that remain unclear, the regions of ascent were more persistent than the regions of descent,
 275 which resulted in the mean ascent observed near $r=0$ above 17 km in Fig. 8b.

276 Vertical advection also played an important role in the tropopause-layer static stability evolution.
 277 Within the eye, subsidence dominated below 17 km, while mean ascent existed near the storm
 278 center above 17 km. Although the magnitude of the subsidence was larger at lower altitudes,
 279 $\partial\theta/\partial z$ was smaller there. Because $\partial\theta/\partial z$ was smaller, the subsidence at lower levels could not
 280 accomplish as much warming as the subsidence at higher levels in the eye, consistent with the
 281 results of Stern and Zhang (2013). As a result, vertical advection within the eye acted to stabilize
 282 the layer below 16 km during RI.

283 Outside of the 27-km radius, ascent dominated the troposphere, while a 1.5-km-deep layer of
 284 descent existed immediately above the tropopause. These regions of ascent and descent converged

just above the tropopause; this convergence acted to compact the isentropes in this layer and increase the static stability. Above the lower-stratospheric subsidence maximum, meanwhile, vertical advection acted to decrease N^2 . In the troposphere, differential vertical advection increased N^2 within the eyewall region and above the vertical velocity maximum at larger radii. Outside of the eyewall and below the vertical velocity maximum, meanwhile, vertical advection acted to decrease N^2 .

Comparing the N^2 tendencies forced by horizontal (Fig. 8a) and vertical (Fig. 8b) advection to the total advective tendency seen in Fig. 6b reveals that horizontal advective tendencies dominated the troposphere, while vertical advective tendencies dominated the layer near and above the tropopause. Thus, tilting of isentropes in the vicinity of the upper-tropospheric outflow maximum appears to be the most important process governing the N^2 tendency in the troposphere, whereas convergence of vertical velocity appears to be the most important process near the tropopause.

b. The role of radiation

During the initial spin-up period (0-24 hours; Fig. 9a), convection was not deep enough to deposit large quantities of ice near the tropopause to create a persistent cirrus canopy. Due to the lack of ice particles, the radiative heating tendencies during this period (Fig. 9b) were relatively small and confined to the region above a few particularly strong, although transient, convective towers. During RI (24-48 hours; Fig. 9b), the eyewall updraft strengthened and a radially-extensive cirrus canopy developed near the tropopause. The enhanced vertical gradient of ice mixing ratio at the top of the cirrus canopy induced strong diurnal-mean radiative cooling near the tropopause (Fig. 9d). This cooling exceeded 0.6 K h^{-1} in some places and sloped downward from the lower stratosphere into the upper troposphere, following the top of the cirrus canopy. A small radiative warming maximum also appeared outside of the 140-km radius below this region of cooling. These

308 results broadly agree with those of Bu et al. (2014; see their Fig. 11a), whose CM1 simulations
309 produced a 0.3 K h^{-1} diurnally-averaged radiative cooling at the top of the cirrus canopy and
310 radiative warming within the cloud that maximized near the 200-km radius. This broad region
311 of radiative cooling acted to destabilize the layer below the cooling maximum and stabilize the
312 layer above, which can be seen in Fig. 6d. The small area of net radiative heating outside of the
313 140-km radius enhanced the destabilization above 16 km in this region and produced a thin layer
314 of stabilization in the 15-16-km layer.

315 After the TC's RI period completed (48-72 hours; Fig. 9f), strong radiative cooling remained
316 near the tropopause at inner radii, sloping downward with the top of the cirrus canopy to below
317 the tropopause at outer radii. Cooling rates exceeded 1 K h^{-1} just above the tropopause between
318 the 30- and 70-km radii. This value is more than three times the maximum cooling rate of 0.3 K h^{-1}
319 observed by Bu et al. (2014), a discrepancy that is a consequence of their larger vertical grid
320 spacing compared to that used here, along with a contribution from differing radiation schemes.
321 To compare our results to those of Bu et al. (2014), we ran a simulation identical to that described
322 in Section 2, except using the NASA-Goddard radiation scheme and 625-m vertical grid spacing,
323 to match those of Bu et al. (2014). This simulation produced a maximum radiative cooling rate
324 of 0.3 K h^{-1} , which agrees with that shown in Bu et al. (2014). Another simulation using 625-m
325 vertical grid spacing and RRTMG radiation produced cooling rates of up to 0.6 K h^{-1} , which is
326 consistent with the WRF simulations of Bu et al. (2014). This suggests that vertical grid spacing
327 smaller than 625 m is necessary to resolve properly the radiative cooling at the top of the cirrus
328 canopy, and that the results can be quite sensitive to the radiation scheme used.

329 Time-mean radiative warming spread from 30- to 160-km radius within the cirrus canopy. The
330 existence of radiative cooling overlying radiative warming in this region led to radiatively-forced
331 destabilization at and below the tropopause, as was observed in Fig. 7d. Beneath the warming

layer existed a region of forcing for stabilization, while a much stronger region of forcing for stabilization existed in the lower stratosphere, above the cooling maximum.

The results herein suggest that radiative heating tendencies played an important role in destabilizing the upper troposphere and stabilizing the lower stratosphere after the cirrus canopy developed.

c. The role of turbulent mixing

Although vertical turbulence always acts to eliminate vertical gradients of θ , this adjustment toward a neutral state only occurs where the mixing takes place. If turbulence occurs in a stably-stratified layer, it will act to decrease θ at the top of the layer and increase it below. Just above and just below the mixed layer, however, the θ profile remains undisturbed. Consequently, although turbulent mixing acts to decrease $\partial\theta/\partial z$ in the layer in which it is occurring, it actually increases $\partial\theta/\partial z$ just below and just above the layer. These vertical gradients of turbulent mixing are quite important, particularly on the flanks of the upper-tropospheric outflow jet.

Two distinct maxima of vertical eddy diffusivity developed in the tropopause layer as the storm intensified (Fig. 10). Comparison of these turbulent regions to the N^2 tendencies in Figs. 6c and 7c reveals that the layers in which vertical eddy diffusivity maximized corresponded to layers of destabilization due to vertical turbulence. Just outside of these layers, however, vertical turbulence acted to increase N^2 . The large vertical gradient of vertical eddy diffusivity near the tropopause played an important role in developing the lower-stratospheric stable layer during RI. This supports the hypothesized role of turbulence in setting the outflow-layer θ stratification in Rotunno and Emanuel (1987).

6. Conclusions

The simulated N^2 evolution shown herein closely matched that observed during the RI of Hurricane Patricia (2015). Three processes dominated the N^2 variability in the upper troposphere and lower stratosphere: advection, radiation, and vertical turbulence. Radiation and vertical turbulence played particularly important roles in developing the strong N^2 maximum just above the cold-point tropopause during RI. Since these two processes are parameterized, and radiation closely depends on yet another parameterized process (microphysics), the tropopause-layer N^2 variability could be quite sensitive to the assumptions inherent to the parameterizations used. A better understanding of the microphysical characteristics of the TC cirrus canopy, its interaction with radiation, and outflow-layer turbulence is critical to understanding the tropopause-layer N^2 evolution.

In this paper, all of the variables were averaged over a full diurnal cycle to eliminate the effects of diurnal variability and isolate the overall storm evolution. Diurnal variations in static stability near the tropopause are potentially of interest with respect to the tropical cyclone diurnal cycle, however, and will be the subject of future work.

Acknowledgments. We are indebted to George Bryan for his continued development and support of Cloud Model 1. We also thank Jeffrey Kepert, Robert Fovell, and Erika Navarro for helpful conversations related to this work. This research was supported by NSF Grant #1636799.

APPENDIX

Sensitivity experiments

The simulations exhibited some sensitivity to the initial thermodynamic profile and the prescribed vertical mixing length. Although the details of the intensification and the tropopause-layer

374 N^2 evolution varied when these quantities were changed, the conclusions of the paper remain
375 unchanged.

376 *a. Sensitivity to the initial thermodynamic profile*

377 A number of sensitivity experiments were conducted using a variety of initial soundings. Chang-
378 ing the initial temperature and humidity profiles affected the timing of the onset of organized deep
379 convection and the rapidity of intensification. In all simulations, however, convection eventually
380 penetrated to the tropopause, at which time vertical turbulence and radiation combined with ad-
381 vection to adjust the N^2 profile toward that which was observed in the control run. By the end of
382 the RI period in every simulation, all three processes were actively modifying the N^2 profile near
383 the tropopause.

384 As an example, 24-hour averages of N^2 are plotted in Fig. A1 for a simulation that was identical
385 to that used in this paper, except the initial sounding was determined by averaging every CFSR
386 grid point within 1000 km of TC Patricia's storm center at 18 UTC 21 October 2015 instead of
387 averaging only within the 100-km radius. Although the lower-stratospheric stable layer developed
388 more slowly and was weaker than that shown in Fig. 4, the overall evolution was quite similar and
389 the same budget terms dominated the N^2 evolution.

390 *b. Sensitivity to the vertical mixing length*

391 The rate of turbulent mixing in the Smagorinsky scheme used herein is highly dependent on a
392 prescribed length scale. The vertical mixing length used in this paper (100 m) was based on the
393 sensitivity experiments of Bryan (2012). Prescribing a smaller mixing length produces smaller
394 θ tendencies due to turbulence, but even with a mixing length on the low end of those tested
395 by Bryan (2012), turbulence still played an important role in the tropopause-layer N^2 evolution.

Fig. A2 shows the 24-hour-averaged contributions of turbulent mixing to the N^2 evolution from a simulation identical to that used in this paper, except with a vertical mixing length of 50 m. At all times, vertical turbulence still played an important role in the tropopause-layer N^2 evolution, particularly during the latter stages of RI (48-72 hours).

References

- Bryan, G. H., 2012: Effects of surface exchange coefficients and turbulence length scales on the intensity and structure of numerically simulated hurricanes. *Mon. Wea. Rev.*, **140**, 1125–1143.
- Bryan, G. H., cited 2018: The governing equations for CM1. [Available online at http://www2.mmm.ucar.edu/people/bryan/cm1/cm1_equations.pdf].
- Bryan, G. H., and R. Rotunno, 2009: The maximum intensity of tropical cyclones in axisymmetric numerical model simulations. *Mon. Wea. Rev.*, **137**, 1770–1789.
- Bu, Y. P., R. G. Fovell, and K. L. Corbosiero, 2014: Influence of cloud-radiative forcing on tropical cyclone structure. *J. Atmos. Sci.*, **71**, 1644–1622.
- Doyle, J. D., and Coauthors, 2017: A view of tropical cyclones from above: The Tropical Cyclone Intensity (TCI) Experiment. *Bull. Amer. Meteor. Soc.*, **98**, 2113–2134.
- Duran, P., and J. Molinari, 2018: Dramatic inner-core tropopause variability during the rapid intensification of Hurricane Patricia (2015). *Mon. Wea. Rev.*, **146**, 119–134.
- Emanuel, K., 2012: Self-stratification of tropical cyclone outflow. Part II: Implications for storm intensification. *J. Atmos. Sci.*, **69**, 988–996.
- Emanuel, K., and R. Rotunno, 2011: Self-stratification of tropical cyclone outflow. Part I: Implications for storm structure. *J. Atmos. Sci.*, **68**, 2236–2249.

417 Iacono, M. J., J. S. Delamere, E. J. Mlawer, M. W. Shephard, S. A. Clough, and W. D. Collins,
 418 2008: Radiative forcing by long-lived greenhouse gases: Calculations with the AER radiative
 419 transfer models. *J. Geophys. Res.*, **113** (D13103).

420 Kepert, J. D., J. Schwendike, and H. Ramsay, 2016: Why is the tropical cyclone boundary layer
 421 not "well mixed"? *J. Atmos. Sci.*, **73**, 957–973.

422 Kimberlain, T. B., E. S. Blake, and J. P. Cangialosi, 2016: Tropical cyclone report: Hurricane
 423 Patricia. National Hurricane Center. [Available online at www.nhc.noaa.gov].

424 Komaromi, W. A., and J. D. Doyle, 2017: Tropical cyclone outflow and warm core structure as
 425 revealed by HS3 dropsonde data. *Mon. Wea. Rev.*, **145**, 1339–1359.

426 Markowski, P. M., and G. H. Bryan, 2016: LES of laminar flow in the PBL: A potential problem
 427 for convective storm simulations. *Mon. Wea. Rev.*, **144**, 1841–1850.

428 Ohno, T., and M. Satoh, 2015: On the warm core of a tropical cyclone formed near the tropopause.
 429 *J. Atmos. Sci.*, **72**, 551–571.

430 Rogers, R. F., S. Aberson, M. M. Bell, D. J. Cecil, J. D. Doyle, J. Morgerman, L. K. Shay, and
 431 C. Velden, 2017: Re-writing the tropical record books: The extraordinary intensification of
 432 Hurricane Patricia (2015). *Bull. Amer. Meteor. Soc.*, **98**, 2091–2112.

433 Rotunno, R., and K. A. Emanuel, 1987: An air-sea interaction theory for tropical cyclones. Part II:
 434 Evolutionary study using a nonhydrostatic axisymmetric numerical model. *J. Atmos. Sci.*, **44**,
 435 542–561.

436 Stern, D. P., and F. Zhang, 2013: How does the eye warm? Part I: A potential temperature budget
 437 analysis of an idealized tropical cyclone. *J. Atmos. Sci.*, **70**, 73–89.

438 Thompson, G., R. M. Rasmussen, and K. Manning, 2004: Explicit forecasts of winter precipitation
439 using an improved bulk microphysics scheme. Part I: Description and sensitivity analysis. *Mon.*
440 *Wea. Rev.*, **132**, 519–542.

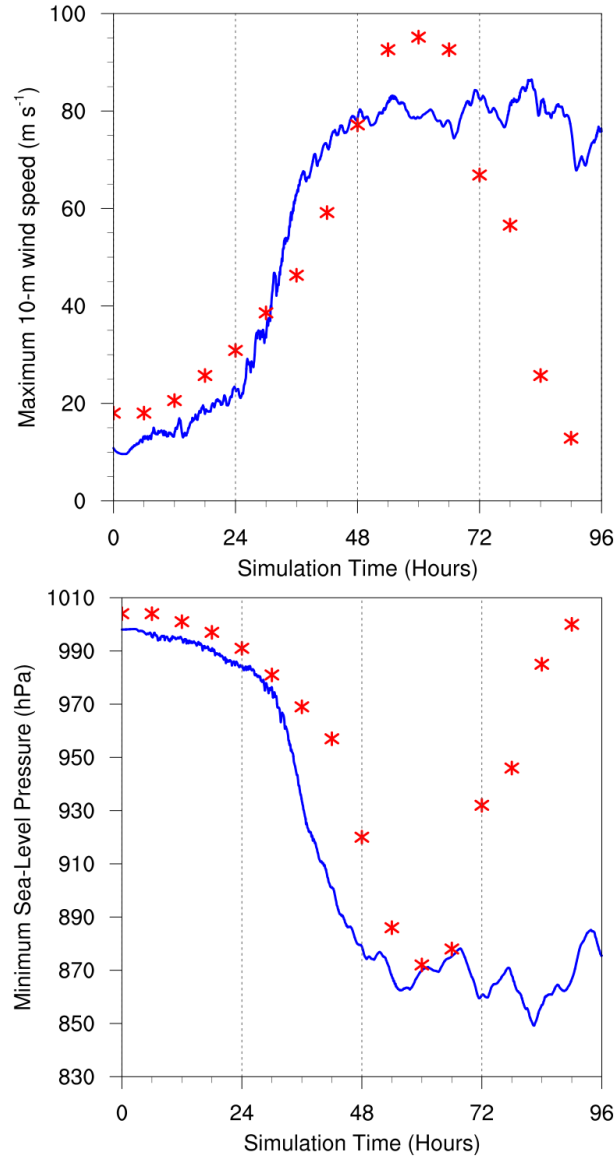
441 Trier, S. B., and R. D. Sharman, 2009: Convection-permitting simulations of the environment sup-
442 porting widespread turbulence within the upper-level outflow of a mesoscale convective system.
443 *Mon. Wea. Rev.*, **137**, 1972–1990.

LIST OF FIGURES

- Fig. 1.** The maximum 10-m wind speed (top panel; m s^{-1}) and minimum sea-level pressure (bottom panel; hPa) in the simulated storm (blue lines; plotted every minute) and from Hurricane Patricia's best track (red stars; plotted every six hours beginning at the time Patricia attained tropical storm intensity). The rapid weakening during the later stage of Patricia's lifetime was induced by landfall. 24
- Fig. 2.** Left panels: Twenty-four-hour changes in squared Brunt-Väisälä frequency (N^2 ; 10^{-4} s^{-2}) computed using Eq. 8 over (top row) 0-24 hours, (middle row) 24-48 hours, (bottom row) 48-72 hours. Middle Panels: The N^2 change over the same time periods computed using Eqs. 4-7, Right Panels: The budget residual over the same time periods, computed by subtracting the budget change (middle column) from the model change (left column). Orange lines represent the cold-point tropopause height averaged over the same time periods. 25
- Fig. 3.** Time series of the contribution of each of the budget terms to the time tendency of the squared Brunt-Väisälä frequency (N^2 ; 10^{-4} s^{-2}). For each budget term, the absolute value of the N^2 tendency is averaged temporally over 1-hour periods (using output every minute), and spatially in a region extending from 0 to 200 km radius and 14 to 21 km altitude. 26
- Fig. 4.** Twenty-four-hour averages of squared Brunt-Väisälä frequency (N^2 ; 10^{-4} s^{-2}) over (a) 0-24 hours, (b) 24-48 hours, (c) 48-72 hours. Orange lines represent the cold-point tropopause height averaged over the same time periods. 27
- Fig. 5.** (a) Total change in N^2 over the 0-24-hour period ($10^{-4} \text{ s}^{-2} (24 \text{ h})^{-1}$) and the contributions to that change from (b) the sum of horizontal and vertical advection, (c) vertical turbulence, (d) longwave and shortwave radiation, (e) the sum of horizontal advection, vertical advection, and vertical turbulence, and (f) the sum of horizontal advection, vertical advection, vertical turbulence, and longwave and shortwave radiation. Orange lines represent the cold-point tropopause height averaged over the 0-24-hour period. 29
- Fig. 6.** As in Fig. 5, but for the 24-48-hour period. 30
- Fig. 7.** As in Fig. 5, but for the 48-72-hour period. 31
- Fig. 8.** The contributions to the change in N^2 over the 24-48-hour period ($10^{-4} \text{ s}^{-2} (24 \text{ h})^{-1}$) by (a) horizontal advection and (b) vertical advection. (c) The radial velocity (m s^{-1} ; filled contours), potential temperature (K; thick black contours), cold-point tropopause height (orange line), and level of maximum outflow (dashed cyan line) averaged over the 24-48-hour period. (d) The vertical velocity (cm s^{-1} ; filled contours), potential temperature (K; thick black contours), and cold-point tropopause height (orange line) averaged over the 24-48-hour period. 32
- Fig. 9.** Ice mixing ratio (g kg^{-1}) and cold-point tropopause height (orange lines) averaged over (a) 0-24 hours, (c) 24-48 hours, and (e) 48-72 hours. Radiative heating rate (K h^{-1}) and cold-point tropopause height (orange lines) averaged over (b) 0-24 hours, (d) 24-48 hours, and (f) 48-72 hours. 34
- Fig. 10.** Vertical eddy diffusivity ($\text{m}^2 \text{ s}^{-2}$; filled contours), cold-point tropopause height (cyan lines), and radial velocity (m s^{-1} ; thick black lines) averaged over (a) 0-24 hours, (b) 24-48 hours, and (c) 48-72 hours. 35

485 **Fig. A1.** Twenty-four-hour averages of squared Brunt-Väisälä frequency (N^2 ; 10^{-4} s^{-2}) over (a) 0-24
 486 hours, (b) 24-48 hours, (c) 48-72 hours, and (d) 72-96 hours for the simulation described
 487 in Appendix Aa. Orange lines represent the cold-point tropopause height averaged over the
 488 same time periods. 36

489 **Fig. A2.** The contribution of vertical turbulence to the N^2 variability ($10^{-4} \text{ s}^{-2} (24 \text{ h})^{-1}$) averaged
 490 over (a) 0-24 hours, (b) 24-48 hours, (c) 48-72 hours, and (d) 72-96 hours for the simulation
 491 described in Appendix Ab. Orange lines represent the cold-point tropopause height averaged
 492 over the same time periods. 37



493 FIG. 1. The maximum 10-m wind speed (top panel; m s^{-1}) and minimum sea-level pressure (bottom panel;
 494 hPa) in the simulated storm (blue lines; plotted every minute) and from Hurricane Patricia's best track (red stars;
 495 plotted every six hours beginning at the time Patricia attained tropical storm intensity). The rapid weakening
 496 during the later stage of Patricia's lifetime was induced by landfall.

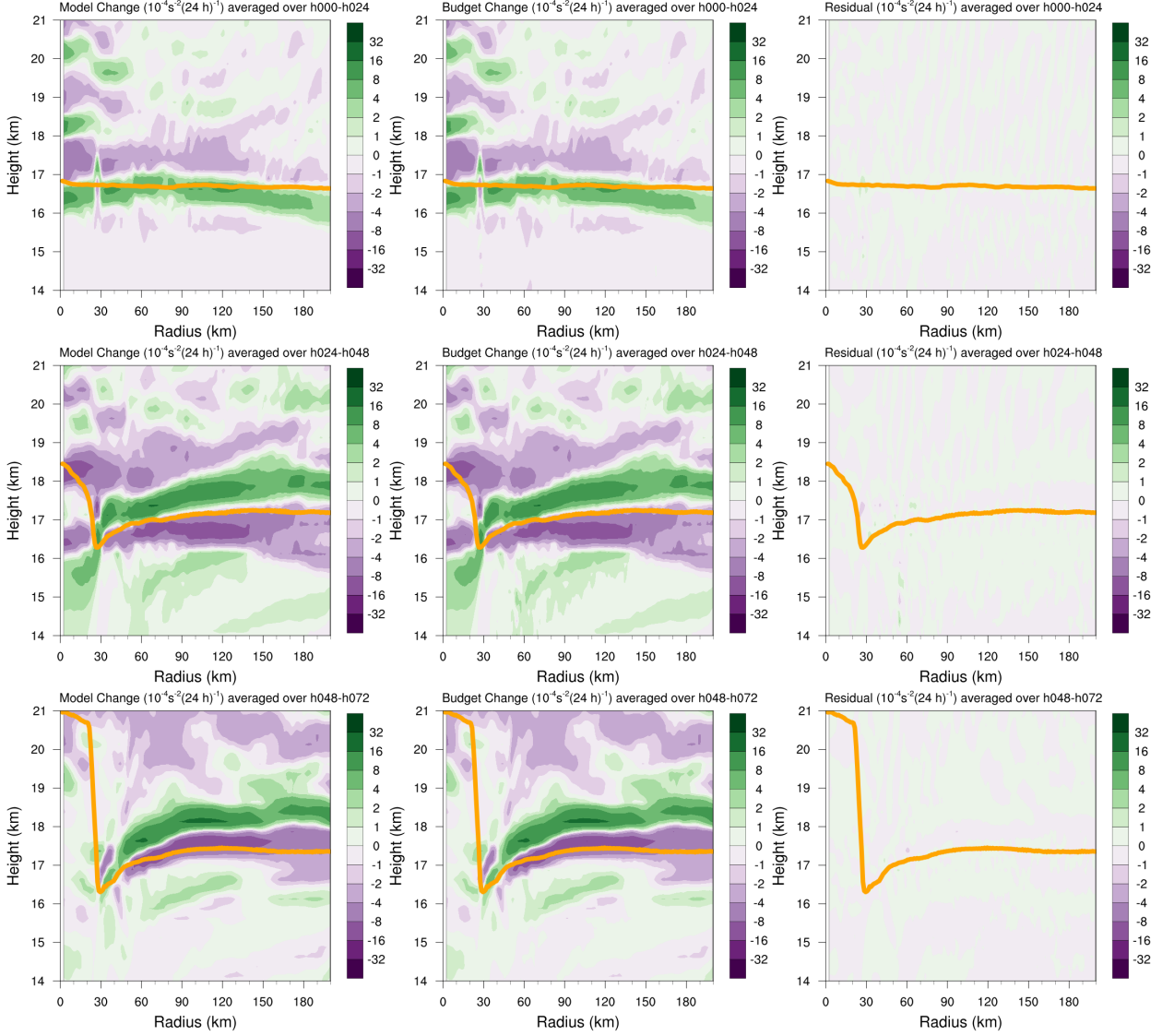


FIG. 2. Left panels: Twenty-four-hour changes in squared Brunt-Väisälä frequency (N^2 ; 10^{-4} s^{-2}) computed using Eq. 8 over (top row) 0-24 hours, (middle row) 24-48 hours, (bottom row) 48-72 hours. Middle Panels: The N^2 change over the same time periods computed using Eqs. 4-7, Right Panels: The budget residual over the same time periods, computed by subtracting the budget change (middle column) from the model change (left column). Orange lines represent the cold-point tropopause height averaged over the same time periods.

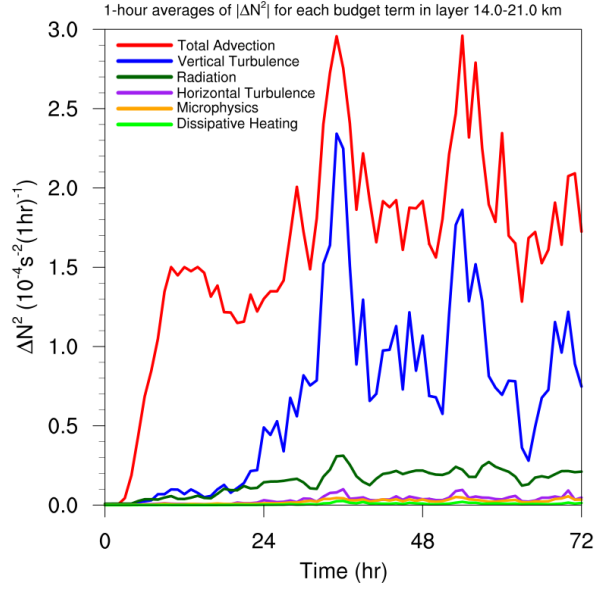


FIG. 3. Time series of the contribution of each of the budget terms to the time tendency of the squared Brunt-Väisälä frequency (N^2 ; 10^{-4} s^{-2}). For each budget term, the absolute value of the N^2 tendency is averaged temporally over 1-hour periods (using output every minute), and spatially in a region extending from 0 to 200 km radius and 14 to 21 km altitude.

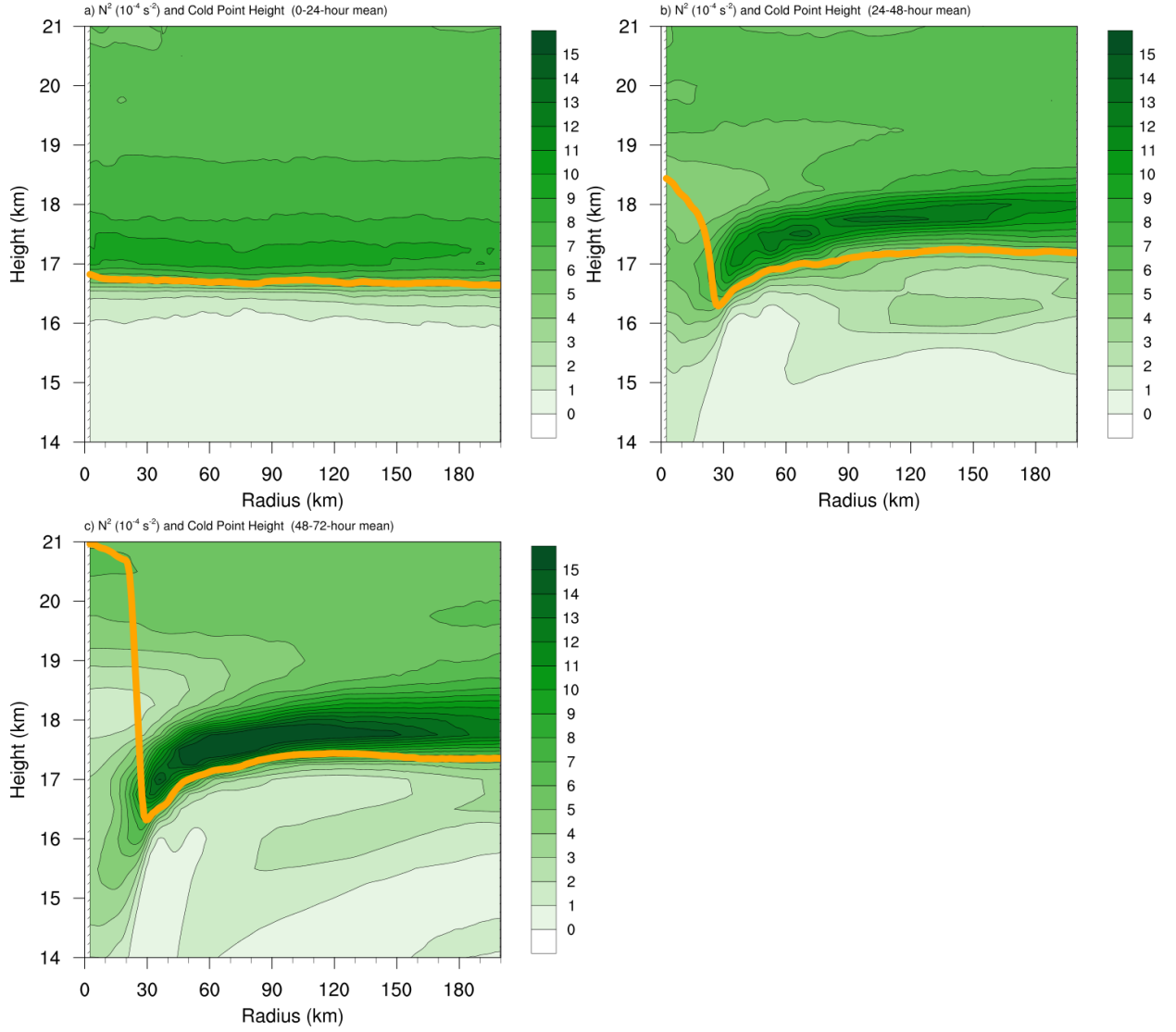
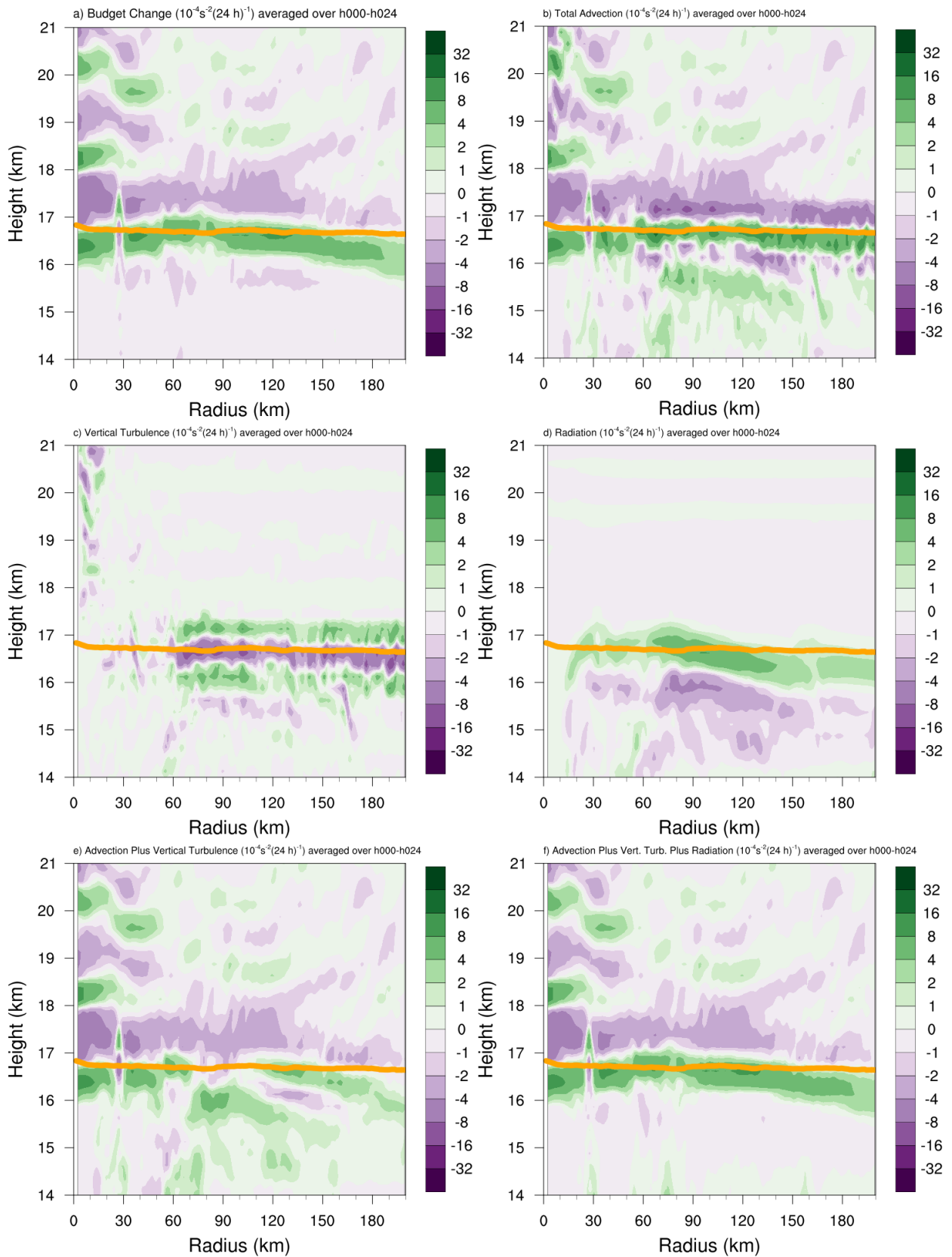


FIG. 4. Twenty-four-hour averages of squared Brunt-Väisälä frequency (N^2 ; 10^{-4} s^{-2}) over (a) 0-24 hours, (b) 24-48 hours, (c) 48-72 hours. Orange lines represent the cold-point tropopause height averaged over the same time periods.



509 FIG. 5. (a) Total change in N^2 over the 0-24-hour period ($10^{-4} \text{ s}^{-2} (24 \text{ h})^{-1}$) and the contributions to that change
 510 from (b) the sum of horizontal and vertical advection, (c) vertical turbulence, (d) longwave and shortwave
 511 radiation, (e) the sum of horizontal advection, vertical advection, and vertical turbulence, and (f) the sum of
 512 horizontal advection, vertical advection, vertical turbulence, and longwave and shortwave radiation. Orange
 513 lines represent the cold-point tropopause height averaged over the 0-24-hour period.

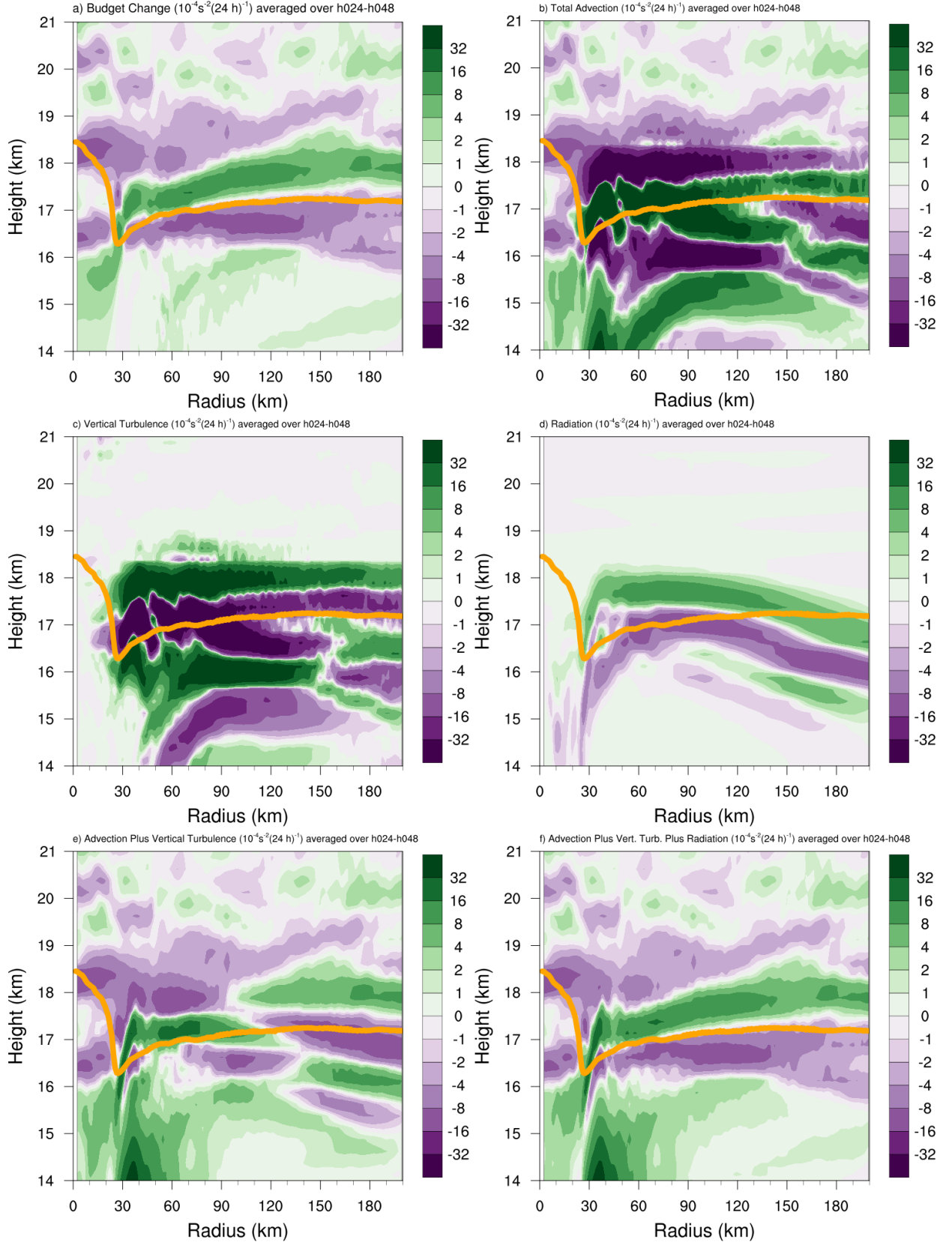


FIG. 6. As in Fig. 5, but for the 24-48-hour period.

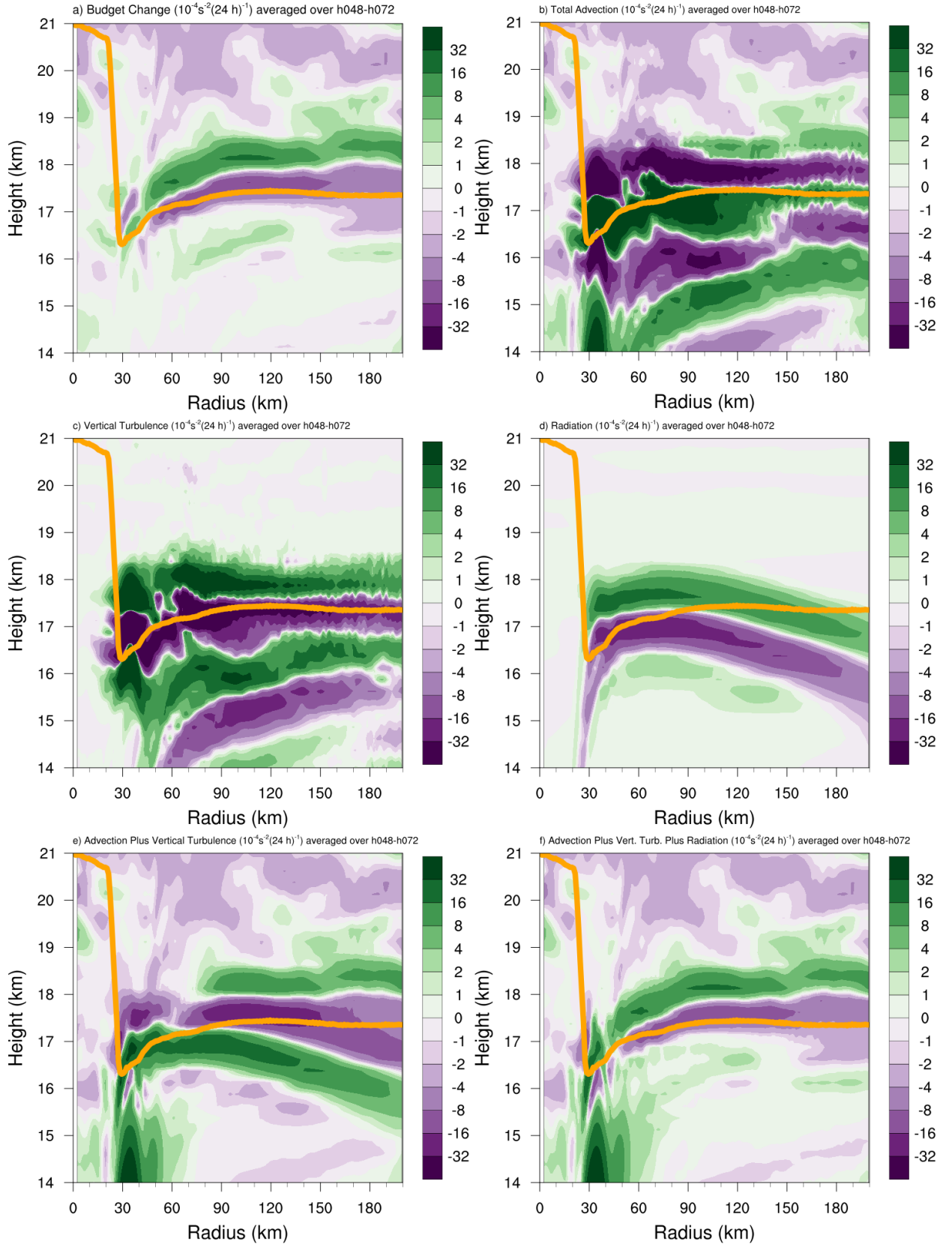


FIG. 7. As in Fig. 5, but for the 48-72-hour period.

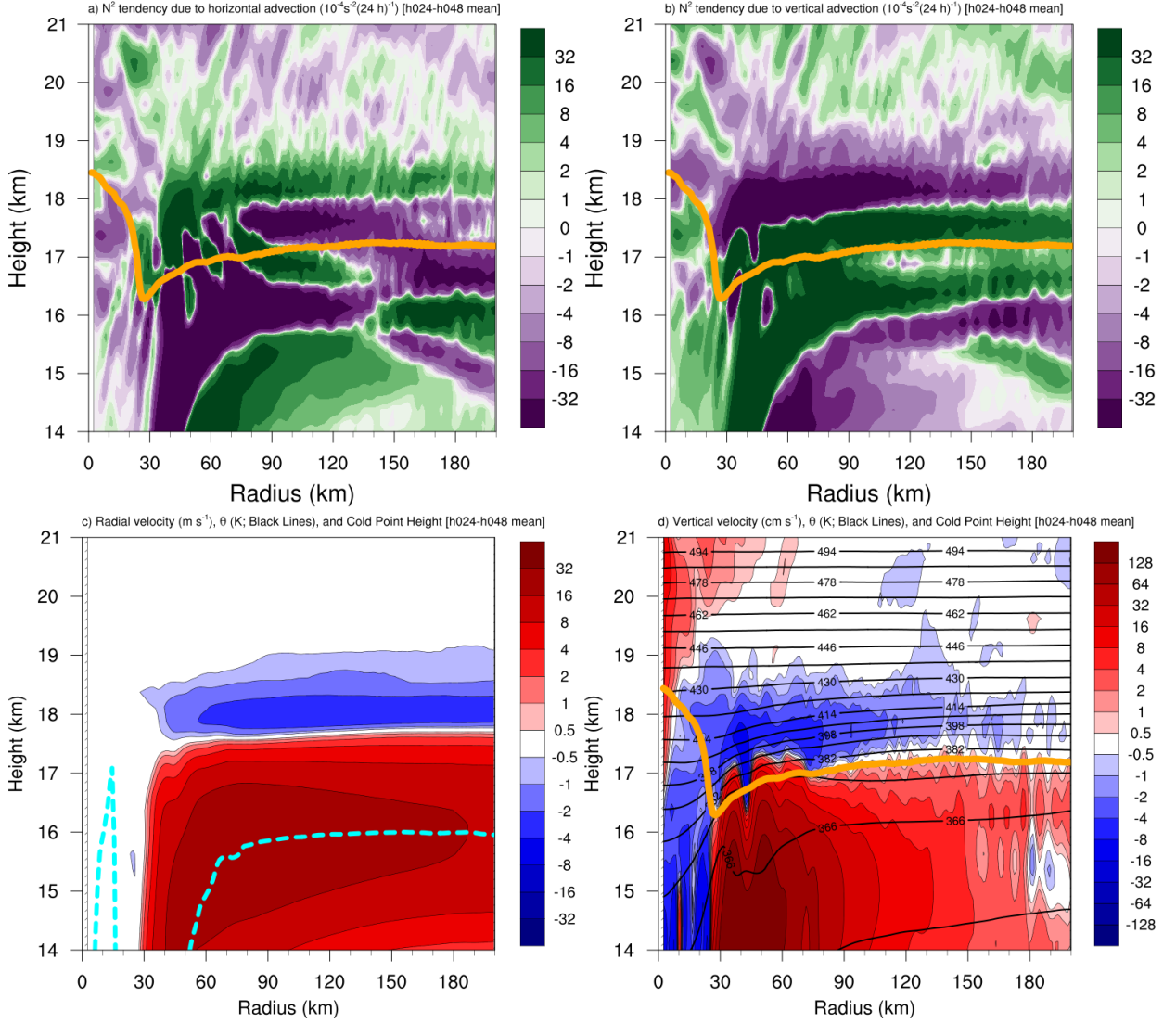
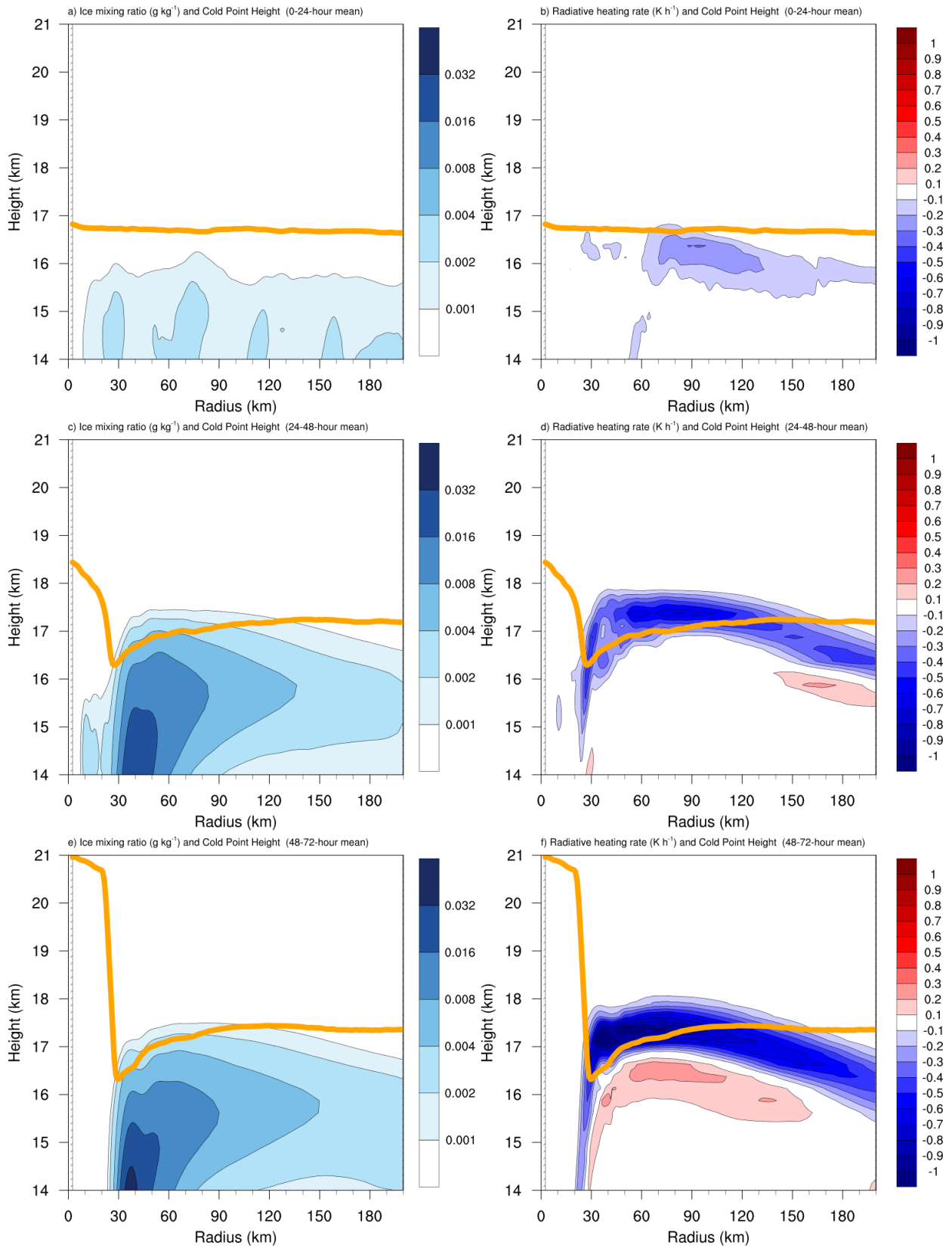


FIG. 8. The contributions to the change in N^2 over the 24-48-hour period ($10^{-4} \text{s}^{-2} (24 \text{ h})^{-1}$) by (a) horizontal advection and (b) vertical advection. (c) The radial velocity (m s^{-1} ; filled contours), potential temperature (K; thick black contours), cold-point tropopause height (orange line), and level of maximum outflow (dashed cyan line) averaged over the 24-48-hour period. (d) The vertical velocity (cm s^{-1} ; filled contours), potential temperature (K; thick black contours), and cold-point tropopause height (orange line) averaged over the 24-48-hour period.



520 FIG. 9. Ice mixing ratio (g kg^{-1}) and cold-point tropopause height (orange lines) averaged over (a) 0-24 hours,
521 (c) 24-48 hours, and (e) 48-72 hours. Radiative heating rate (K h^{-1}) and cold-point tropopause height (orange
522 lines) averaged over (b) 0-24 hours, (d) 24-48 hours, and (f) 48-72 hours.

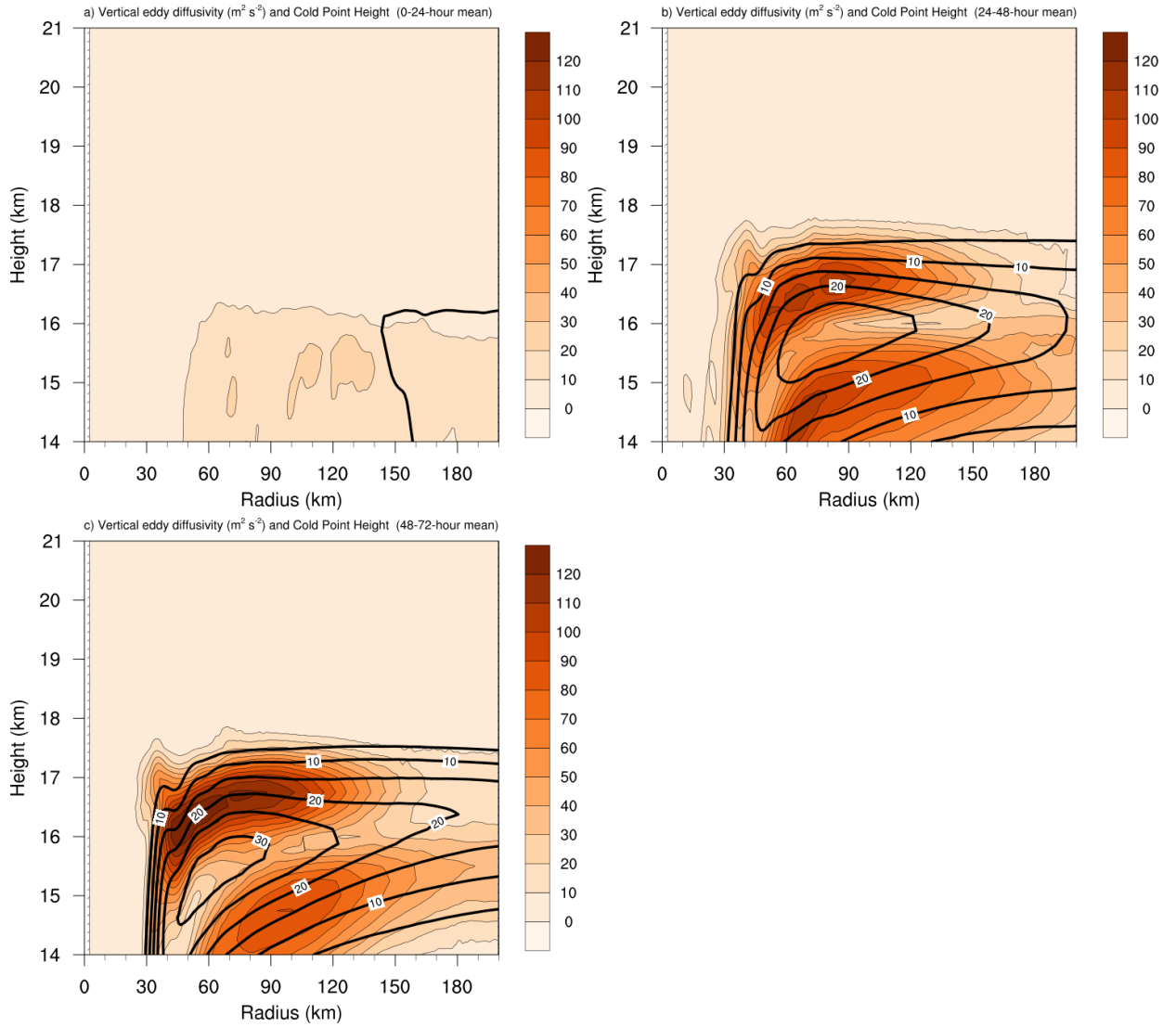
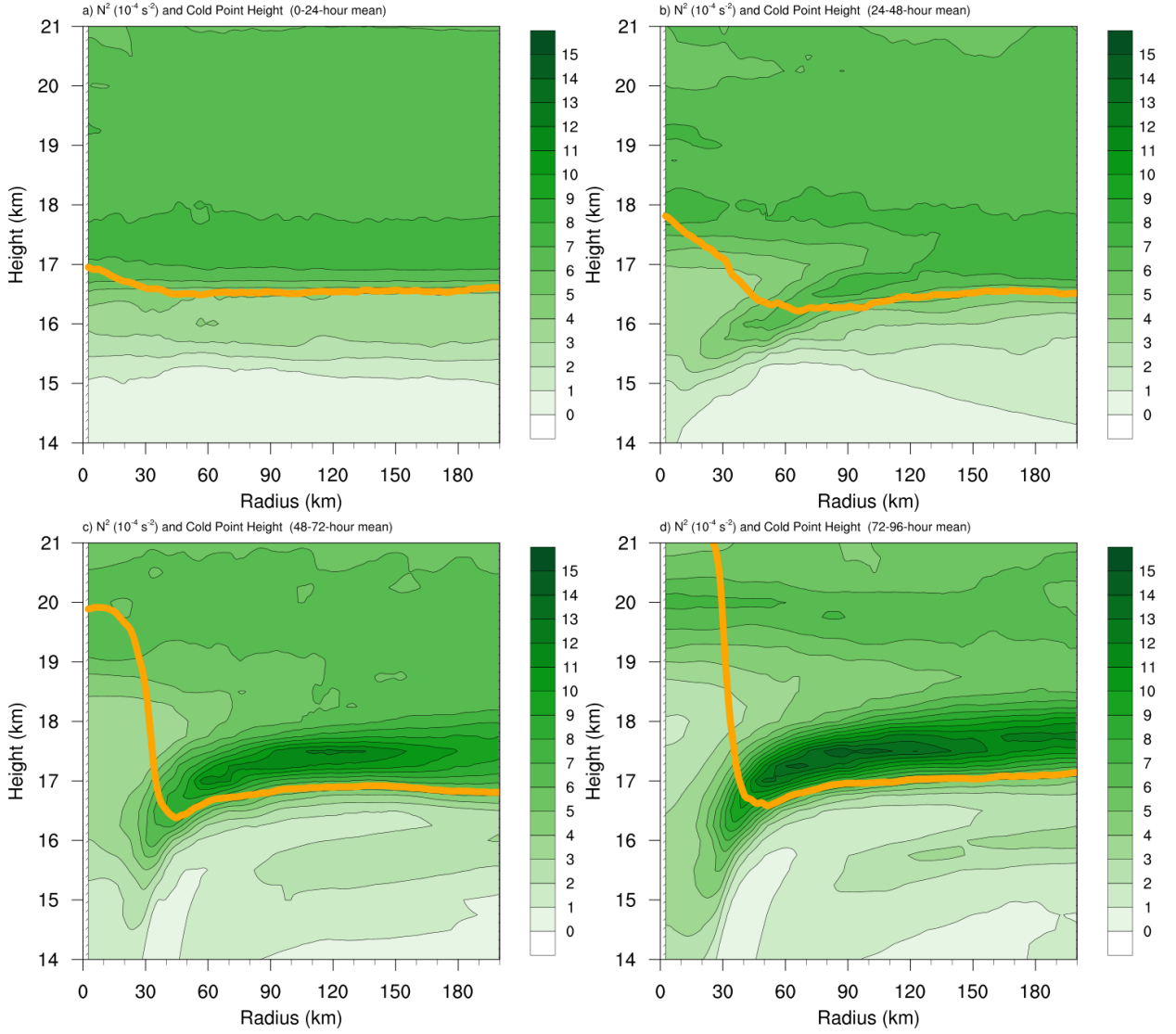


FIG. 10. Vertical eddy diffusivity ($\text{m}^2 \text{s}^{-2}$; filled contours), cold-point tropopause height (cyan lines), and radial velocity (m s^{-1} ; thick black lines) averaged over (a) 0-24 hours, (b) 24-48 hours, and (c) 48-72 hours.



525 Fig. A1. Twenty-four-hour averages of squared Brunt-Väisälä frequency (N^2 ; 10^{-4} s^{-2}) over (a) 0-24 hours,
 526 (b) 24-48 hours, (c) 48-72 hours, and (d) 72-96 hours for the simulation described in Appendix Aa. Orange lines
 527 represent the cold-point tropopause height averaged over the same time periods.

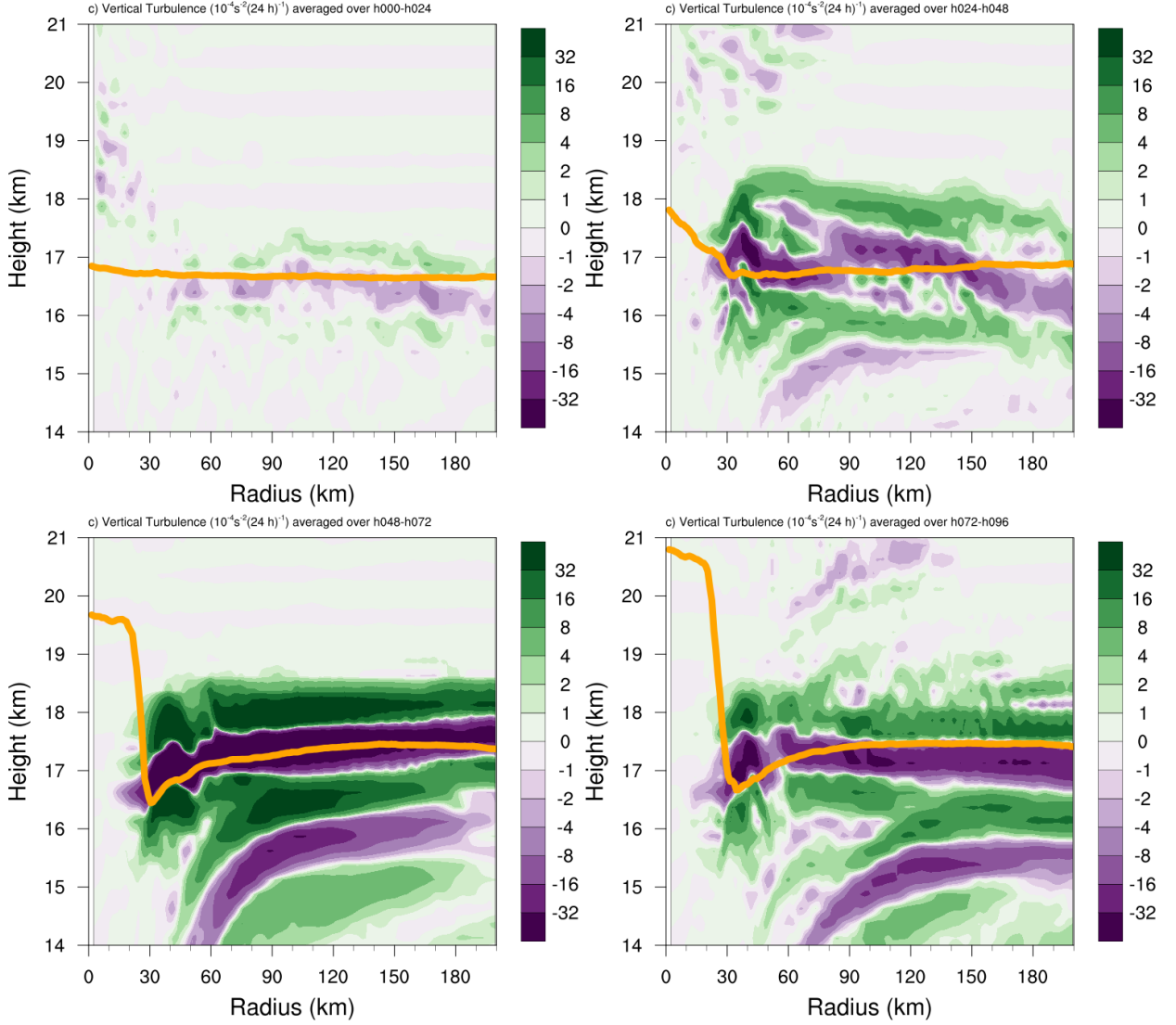


Fig. A2. The contribution of vertical turbulence to the N^2 variability ($10^{-4} \text{ s}^{-2} (24 \text{ h})^{-1}$) averaged over (a) 0-24 hours, (b) 24-48 hours, (c) 48-72 hours, and (d) 72-96 hours for the simulation described in Appendix Ab. Orange lines represent the cold-point tropopause height averaged over the same time periods.